Towards Metal-free Photocatalysis: Photochemical Regeneration of Organic Hydride Donors Using Phenazine-based Photosensitizers

Ravindra B. Weerasooriya, <sup>1,2</sup>, Matthew C. Drummer, <sup>1,2</sup> Brian T. Phelan, <sup>2</sup> Jonathan L. Gesiorski, <sup>1,2</sup> Emily A. Sprague-Klein, <sup>2</sup> Lin X. Chen, <sup>2,3</sup> and Ksenija D. Glusac\*, <sup>1,2</sup>

<sup>1</sup>Department of Chemistry, University of Illinois at Chicago, Chicago, Illinois 60607, United States

<sup>2</sup>Chemical Sciences and Engineering, Argonne National Laboratory, Illinois, 60439, United States

<sup>3</sup>Department of Chemistry, Northwestern University, Evanston, Illinois 60208, United States

**Key Words:** Photo-regeneration, charge transfer, NADH, benzimidazole, organic hydrides, CO<sub>2</sub> reduction, metal-free.

Corresponding author's email: glusac@uic.edu

#### **Abstract**

Earth-abundant chromophores and catalysts are important molecular building blocks for artificial photosynthesis applications. Our team previously reported that metal-free hydride donors, such as biomimetic benzoimidazole-based motifs, can reduce CO<sub>2</sub> selectively to the formate ion and that they can be electrochemically regenerated using the proton-coupled mechanism. To enable direct utilization of solar energy, we report here the photochemical regeneration of a benzoimidazole-based hydride donor using a phenazine-based metal-free chromophore. The photochemical regeneration was investigated under different experimental conditions involving varying sacrificial donors, proton donors, solvents and component concentrations. The best hydride regeneration yield of 50% was obtained with phenol as a proton source and thiophenolate as a sacrificial electron donor. The mechanism of photochemical regeneration was studied using steady-state and time-resolved UV/Vis spectroscopies. Based on the results of these studies, we hypothesize that the initial photoinduced electron transfer from photoexcited phenazine chromophores involves the benzoimidazole cation and that this process is likely coupled with proton transfer to generate protonated benzoimidazole-based radical cation. The second

photoinduced electron transfer is hypothesized to generate the hydride form. Our findings provide the requisite information for the future development of reductive photocatalysts for solar energy and light-harvesting applications utilizing earth-abundant metal-free materials.

#### Introduction

Metal-free hydride donors are important reducing agents in biochemical and chemical transformations. In natural photosynthesis, dihydronicotinamide-adenine dinucleotide phosphate (NADPH) is a key metal-free hydride donor that reduces fixed CO<sub>2</sub> to carbohydrates.<sup>1,2</sup> This process is part of the Calvin-Benson cycle and involves a reduction of 1,3-bisphosphoglycerate to form glyceraldehyde-3-phosphate by NADP-glyceraldehyde phosphate dehydrogenase, which is further converted into carbohydrates. Another example of enzymatic hydride transfer by metalfree hydrides can be found in ketoreductases, where dihydronicotinamide-adenine dinucleotide (NADH) serves to reduce carbonyl groups with exceptional enantioselectivity.<sup>3,4</sup> Ketoreductases are now used on industrial scales for the synthesis of chiral compounds for pharmaceuticals and have fully replaced chemical metal-ligand based catalysts.<sup>4</sup> In addition to enzymatic hydride transfer, many NADH analogs, such as Hantzsch esters, are utilized as stoichiometric metal-free hydride donors for the reduction of C=O, C=C and C=N functional groups in organic synthesis.<sup>5,6</sup> Metal-free hydride donors and their conjugate hydride acceptors are also used as components of frustrated Lewis pairs, which comprise a sterically hindered hydride acceptor (Lewis acid) and a proton acceptor (Lewis base) and are used as a new class of catalysts for hydrogen activation and substrate hydrogenation.<sup>7</sup>

Regeneration of NADH analogs from the corresponding cations is challenging, because of the high energetic penalty associated with the formation of one and two-electron reduced intermediates.<sup>8</sup> Furthermore, the one-electron reduced NAD-radical is chemically unstable, due to high dimerization rates.<sup>8</sup> Nature addresses this challenge by using a flavin-based hydride donor as a mediator for NADPH regeneration, as occurs in Ferrodoxin-NADP+ reductase (Photosystem I).<sup>1</sup> In chemical systems, the regeneration of NADH analogs is rarely achieved and these reductants are often used in stoichiometric rather than catalytic quantities. However, several approaches have recently been demonstrated to successfully regenerate NADH and its analogs using chemical, electrochemical and photochemical methods.<sup>9–15</sup> These approaches often employ hydride

mediators analogous to the flavin-based cofactors found in natural NADPH regeneration. Flavin mediators can form reduced hydride forms without passing through high-energy intermediates or undergoing unwanted side reactions. Such efficient hydride formation is often achieved via proton-coupled electron transfer, a mechanism frequently utilized in natural and artificial redox catalysis to reduce the energy requirements for desired reduction or oxidation processes. For example, Rh(III) complexes are often used as hydride mediators, since they can be reduced to the corresponding hydrides via a proton-coupled mechanism at mild driving forces. 19

Our group investigated catalytic CO<sub>2</sub> reduction to formate using biomimetic NADH-analogs (Scheme 1). Direct CO<sub>2</sub> reduction by 1-benzyl-1,4-dihydronicotinamide (BNAH), a biomimetic model of the NADPH cofactor in photosynthesis, is endergonic, <sup>20,21</sup> indicating that stronger hydride donors are needed to enable spontaneous reduction of CO<sub>2</sub> to formate. For this reason, we determined, both experimentally and computationally, thermodynamic hydricities of NADHanalogs to identify derivatives with hydricity values that are smaller than that of the formate ion  $(\Delta G_{H} = 44.0 \text{ kcal/mol})$  in ACN, 42 kcal/mole in DMSO).<sup>20</sup> Our structure-property relationships have shown that strong metal-free hydride donors can be prepared by the introduction of structural elements that stabilize cations formed upon the hydride ion release (such as extended charge delocalization and electron donating substituents). 16,21 Benzimidazole-based hydrides, such as MeBIMH in Scheme 1, were identified as thermodynamically suitable donors for CO<sub>2</sub> reduction and this finding was confirmed in a follow-up study, where the formate ion formation was detected and quantified, providing the first proof-of-principle study illustrating the ability of NADHanalogs to reduce CO<sub>2</sub><sup>22</sup>, albeit with sluggish kinetics.<sup>23</sup> The regeneration of NADH analogs was investigated using electrochemical methods and this study demonstrated that the quantitative hydride regeneration can be achieved for selected NADH analogs, whose radical cations exhibit pKa values that enable proton-coupled reduction. 8 Such proton-coupled mechanism was found to not only lower the electrochemical potential at which the regeneration occurs, but also to prevent the undesired dimerization of one-electron reduced radicals. Our attempts to photochemically regenerate NADPH-analogs were limited to dye-sensitized approaches, where GaP and NiO semiconductors were used as hole acceptors.<sup>24,25</sup> These studies showed limited success, because of the inadequate visible light absorption by open-shell NAD analog intermediates and because of the fast charge recombination following the initial photoexcitation and charge separation.

**Scheme 1:** Reduction of CO<sub>2</sub> to formate by organic hydrides R-H, such as NADH, BNAH and MeBIMH. The hydride regeneration step involving a transfer of two electrons and a proton is shown to illustrate the relevant thermodynamic parameters. Hydridic hydrogens are shown in red.

$$CO_{2} + R-H \longrightarrow R^{+} + HCOO^{-}$$

$$E_{2 (red)} \uparrow \qquad \downarrow E_{1 (red)}$$

$$RH \longrightarrow PKa \qquad R^{*}$$

$$R \mapsto PKa \qquad \downarrow E_{1 (red)}$$

$$R \mapsto PKa \qquad$$

In this study, we investigate the photochemical regeneration of benzimidazole-based hydride donors using molecular photosensitizers (Scheme 2). N,N-di(2-naphthyl)-5,10-dihydrophenazine chromophore (PC1) was selected for this work, because it and similar phenazine and phenoxazinebased chromophores were shown previously by Miyake and co-authors to exhibit strongly reducing excited states, <sup>26–28</sup> high intersystem crossing yields, long-lived triplet charge-transfer excited states<sup>27–29</sup> and strong absorption that extends into the visible region<sup>26–30</sup>. These metal-free chromophores have been utilized in many photochemical transformations, including trifluoromethylations<sup>27</sup>, Ni-catalyzed C-N and C-S coupling reactions<sup>27</sup>, C-H fluoroalkylation reactions<sup>31</sup>, organocatalyzed atom transfer radical polymerization<sup>26,28,30</sup>, and CO<sub>2</sub> reduction catalysis<sup>32</sup>. The photochemical conversion of organic hydride acceptor BIM<sup>+</sup> to the corresponding reduced BIMH form was investigated in the presence of different sacrificial electron and proton donors. We find that the maximum regeneration yield of 50% was achieved under optimized conditions and we hypothesize that further improvements can be achieved with the appropriate selection of the sacrificial donor. Our steady-state and time-resolved spectroscopic investigations indicate that the photochemical reaction is initiated by a photoinduced electron transfer from the S<sub>1</sub> state of PC1 to BIM<sup>+</sup>. We anticipate that this work will be of relevance for the development of future earth-abundant reduction photocatalysts.

**Scheme 2.** Photochemical regeneration of organic hydride BIMH with an organic chromophore PC1 in the presence of thiol-based sacrificial donors SD1 and SD2. "\*" denotes the excited state.

$$SD1 = \bigcap_{S}^{S^{-}}$$

$$SD2 = \bigcap_{S}^{N}$$

$$PC1$$

#### Methods

Methods and materials. All chemicals were purchased from commercial suppliers and used without further purification unless otherwise noted. Absorption spectra were measured with either a Cary 300 (Agilent), DU 800 (Beckman Coulter), or Ocean FX (Ocean Optics) spectrophotometer. The fluorescence experiments were collected on FluoroMax 4 (Horiba) spectrofluorometer in a 1 cm quartz cell. <sup>1</sup>H and <sup>13</sup>C NMR spectra were collected on an Avance III 500 MHz system (Brucker). BIM<sup>+</sup> (counter anion is ClO<sub>4</sub><sup>-</sup>) was synthesized according to the previously published procedure. <sup>1</sup> PC1, SD1 (tetrabutylammonium thiophenolate or sodium thiophenolate) and SD2 (diethyldithiocarbamic acid diethylammonium salt and sodium diethyldithiocarbamate) were purchased from Sigma-Aldrich.

Electrochemistry. Cyclic voltammetry was performed using a BASi epsilon potentiostat in a VC-2 voltammetry cell (Bioanalytical Systems) using platinum working electrode (1.6 mm diameter, MF-2013, Bioanalytical Systems), a non-aqueous Ag/Ag<sup>+</sup> reference electrode (MF-2062, Bioanalytical Systems), and a platinum wire (MW-4130, Bioanalytical Systems) as a counter electrode. Electrochemical potentials were referenced to NHE by adding 0.548 V to the experimental potentials.<sup>33</sup> Spectroscopic grade DMSO and the electrolyte tetrabutylammonium perchlorate (TBAP) were purchased from Sigma Aldrich and used without further purification.

**Bulk Electrolysis.** Electrolysis of BIM<sup>+</sup> was performed in a glovebox using a BASi Epsilon potentiostat in a VC2 voltammetry cell (Bioanalytical Systems), with a carbon fiber paper working electrode (Freudenberg H23, Fuel Cell Store), a nonaqueous Ag/Ag<sup>+</sup> reference electrode (MF-2062, S14 Bioanalytical Systems), and a coiled platinum wire in an auxiliary electrode chamber (MW-1033 and MR1196, Bioanalytical Systems) as the counter electrode. The electrolysis was performed in deuterated DMSO-d<sub>6</sub>, while the progress was monitored using <sup>1</sup>H NMR spectroscopy.

**Spectroelectrochemistry.** The spectroelectrochemistry of PC1 was performed using Pt mesh working electrode (EF-1365, Bioanalytical Systems), non-aqueous Ag/Ag<sup>+</sup> reference and Pt wire as an auxiliary electrode. A solution of 1 mM PC1 in acetonitrile containing 0.1 M TBAP was purged with argon prior to the experiment. Changes in the absorption were monitored on an Ocean FX Miniature spectrometer (Ocean Optics) in 10 s intervals after applying a potential of 0.8 V vs. NHE.

**Photochemical regeneration of BIMH.** Photo regeneration of BIMH was conducted in a fluorescence cuvette (4 mL) closed with a sealed cap. Samples were prepared in an inert atmosphere and the volume of the solution in each cuvette was 3 mL and contained 1.0 mM PC1,  $10\text{-}50 \text{ mM BIM}^+$ , 0.05-0.2 M proton source and 50-300 mM sacrificial electron donor in benzene: DMF (1:1) solvent mixture. The solution was then irradiated by blue LED ( $\lambda = 460 \text{ nm}$ ). The products were analyzed by using  $^1\text{H-NMR}$  and quantified by integrating the peak intensities of BIM+ (3.85 ppm) and BIMH (3.40 ppm) before and after the reaction.

## Time-resolved laser spectroscopy.

Femtosecond transient absorption spectroscopy. The setup used here consists of a mode-locked Ti:sapphire oscillator and regenerative amplifier (Astrella, Coherent Inc.) operating at a repetition rate of 1 kHz to generate a 100 fs pulsed beam centered at 800 nm. The output beam was split into pump and probe beams. The pump beam was sent to an optical parametric amplifier (OPerA Solo, Coherent Inc.) to obtain the desired wavelength of the pump beam. The probe beam was focused into a 4mm CaF<sub>2</sub> crystal to generate a 350-750 nm white light continuum which was continuously translated with a linear stage (Newport MFA-CC) to avoid damage to the crystal. The angle between pump and probe polarizations was set to 54.7° to eliminate the effect of molecular rotations on the kinetics. After transmitting through the sample, the probe beam was directed into an optical fiber and input into a CCD spectrograph (Ocean Optics, Flame-S-UV-VIS-ES). Data

acquisition was performed using custom LabVIEW (National Instruments) software. Data processing (background subtraction, outlier removal, and averaging) were done in a custom LabView data processing program, while chirp correction was performed via CarpetView (Light Conversion). Global fitting analysis was performed using the global analysis function in CarpetView. Reported time constants with standard deviations were calculated as averages from three separate data sets. Numerous sequential models were tested, and their quality evaluated based on the agreement between the calculated component spectra and the time-resolved evolution of the fsTA spectra.

Samples were prepared by adding solid sample powder to the appropriate organic solvent mixture of 1:1 benzene:DMF (0.001 g/mL). Mild sonication was used to fully dissolved the solids. Samples were kept in a 2 mm quartz cuvette for steady-state absorption and transient absorption spectroscopies.

Nanosecond transient absorption spectroscopy. Nanosecond transient absorption (nsTA) spectroscopy experiments were performed using a previously described Nd:YAG laser system (PL2210 oscillator and amplifier / PG403 optical parametric generator, Ekspla) coupled to a supercontinuum laser (STM-1-UV, Leukos).<sup>34</sup> Briefly, the amplifier output a 0.5 kHz train of 355 nm, 25 ps, 0.3 mJ pulses that pumped the optical parametric generator tuned to output 430 nm (25 ps, 25-50 µJ) pump pulses. DG535 delay generators (Stanford Research Systems), triggered by the 1 kHz master trigger from the PL2210 amplifier, triggered the supercontinuum laser at prescribed time delays ranging from -50 ns to +950 µs. The supercontinuum laser output a 1 kHz train of broadband (400-1600 nm, 600 ps, 15 μJ) probe pulses generated in a 2 m photonic crystal fiber. The pump was attenuated to 500 nJ/pulse and focused to about 200-300 µm at the sample. The broadband probe was attenuated with a neutral density filter, directed through a 950 nm shortpass filter to remove residual fundamental (1064 nm), and focused to about 150 µm at the sample. After interacting with the sample, the probe and signal were detected using an SP-2150i Acton Series spectrograph (Princeton Instruments) coupled with a Spyder3 SG-14 (Teledyne DALSA) CCD camera. A laboratory-written application (LabVIEW 2014, National Instruments) provided the time delays to the delay generators, recorded the probe spectra, and calculated the difference signal. The nsTA data were corrected for scan-to-scan drift in the pump-probe timing provided by the delay generators, had the background signal (scattered pump photons and long-lived, >1 ms,

transient signals) subtracted, and were corrected for group delay dispersion (GDD) in the probe pulses.

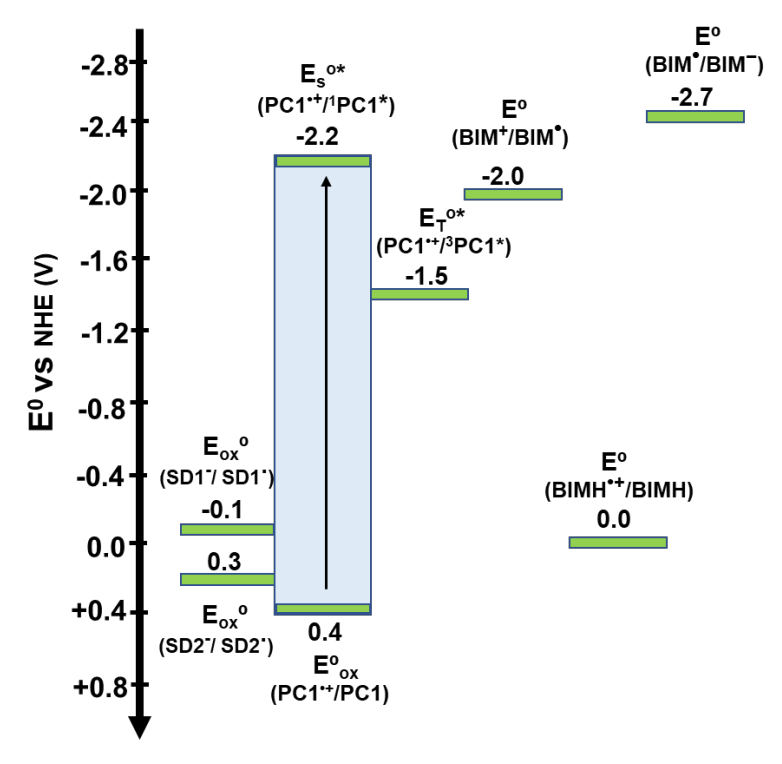
0.5 mM of PC1, 0.5 mM PC1 and 25 mM BIM<sup>+</sup>, 0.5 mM, 25 mM BIM<sup>+</sup> and 0.1 M Phenol, 0.5 mM PC1, and 60 mM SD1 samples were prepared in 1:1 N,N-dimethylformamide (DMF)/benzene in 1 cm quartz cuvettes for the nsTA spectroscopy experiments. The nsTA samples were prepared to eliminate the effects of oxygen on the measured dynamics. Oxygen-free samples were prepared in an inert atmosphere.

## **Results and Discussion**

Thermodynamics of photoinduced electron transfer. The regeneration of benzimidazole-based hydride donors requires highly reducing conditions.<sup>8</sup> For example, the standard reduction potentials for BIM<sup>+</sup>/BIM<sup>-</sup> and BIM<sup>-</sup>/BIM<sup>-</sup> couples are -2.0 and -2.7 V vs NHE<sup>8</sup> (Scheme 2). We have shown previously that, in the presence of a suitable proton source, the regeneration energy requirements are lowered, since the protonated BIMH<sup>•+</sup>, formed in the presence of a proton source, exhibits reduction at 0.0 V vs NHE (Scheme 2).8 Thus, the reduction of BIM<sup>+</sup> in the presence of a proton source requires a photosensitizer with excited-state reduction potential that is more negative than -2.0 V vs NHE. The organic photosensitizer PC1 was selected for this study because the standard reduction potential of PC1 in the  $S_1$  excited state is estimated to be -2.2 V vs NHE, which is sufficiently reducing for our study (Scheme 2). Furthermore, previous studies showed that <sup>1</sup>PC\* is long-lived (in THF, singlet excited state lifetime is 21.5 ns, while the triplet excited-state lifetime is 15.2 µs),<sup>35</sup> which is advantageous for the photoreduction of BIM<sup>+</sup> described in Scheme 2.<sup>35</sup> While the one-electron reduced radical forms of benzimidazoles tend to undergo radical dimerization, the presence of bulky methoxy groups in BIM+ were shown to stabilize BIM, leading to electrochemically reversible cyclic voltammograms. 8 Sulfur-based compounds SD1 and SD2 were selected as sacrificial electron donors to regenerate PC1, because they are sufficiently reducing (Scheme 2).36,37

**Scheme 3.** Standard reduction potentials for the compounds used in this study. The ground-state reduction for PC1, E°(PC1 $^{++}$ /PC1) was obtained from a reference.<sup>27</sup> The corresponding value for the S<sub>1</sub> standard reduction potential of PC1 (E<sub>s</sub>°\*(PC1 $^{++}$ /PC1) was obtained using experimental ground-state potential<sup>27</sup> and the midpoint between UV/vis absorption (at 345 nm) and emission (592 nm) peaks of PC1 (Figure 1), while the value for the T<sub>1</sub> standard reduction potential of PC1

 $(E_T^{o*}(PC1^{\bullet+}/PC1))$  was obtained from a reference value.<sup>27</sup> The reduction potentials for BIMH derivatives and sacrificial donors were obtained from the references.<sup>8,36,37</sup>



Steady-state spectroscopy. UV/vis absorption spectra of model compounds are shown in Figure 1a. The absorption of PC1 appears in the 315-460 nm wavelength range and the peak and shoulder features are assigned to the  $S_0 \rightarrow S_4$  (350 nm) and  $S_0 \rightarrow S_2$  (425 nm) transitions, respectively.<sup>38</sup> Given that charge-transfer excited-state energies tend to be sensitive to the solvent polarity, we performed photochemical experiments in a benzene/DMF solvent mixture that is sufficiently nonpolar to preserve the strong reducing power of PC1 excited state,<sup>39</sup> and at the same time polar enough to solubilize ionic compounds (BIM<sup>+</sup>, SD1 and SD2). The absorption spectrum of PC1 extends into the blue part of the visible range (up to ~450 nm), while other model compounds absorb predominantly in the UV-range, making the PC1 compound an accessible excited-state reductive photocatalyst operable within the visible spectral range. Thus, 430 nm light was used for the emission quenching experiments shown in Figures 1b and 1c. An example quenching experiment of the PC1 excited state is shown in Figure 1b, where BIM<sup>+</sup> was used as an electron acceptor. The PC1 emission spectrum consists of a broad structureless emission band with  $\lambda_{max}$  =592 nm, which has been previously assigned to the emission from the S<sub>1</sub> charge-transfer state of PC1.<sup>39</sup> In the presence of increasing amounts of BIM<sup>+</sup>, the intensity of the 592 nm emission band

decreases, likely due to excited-state quenching via electron transfer from excited PC1 to BIM<sup>+</sup>. The fluorescence was not completely quenched, because of the limited solubility of BIM<sup>+</sup> in the solvent mixture of choice. Quenching experiments were also performed with SD1 and SD2 (Figure S1-S3) and the resulting Stern-Volmer plots are shown in Figure 1c. The resulting quenching rate constants are  $\sim 3 \cdot 10^9$  M<sup>-1</sup>s<sup>-1</sup>, indicating the quenching processes are diffusion controlled upon photoexcitation of PC1. At the upper limits of the quencher concentrations, the quenching efficiencies were found to be about 52%.

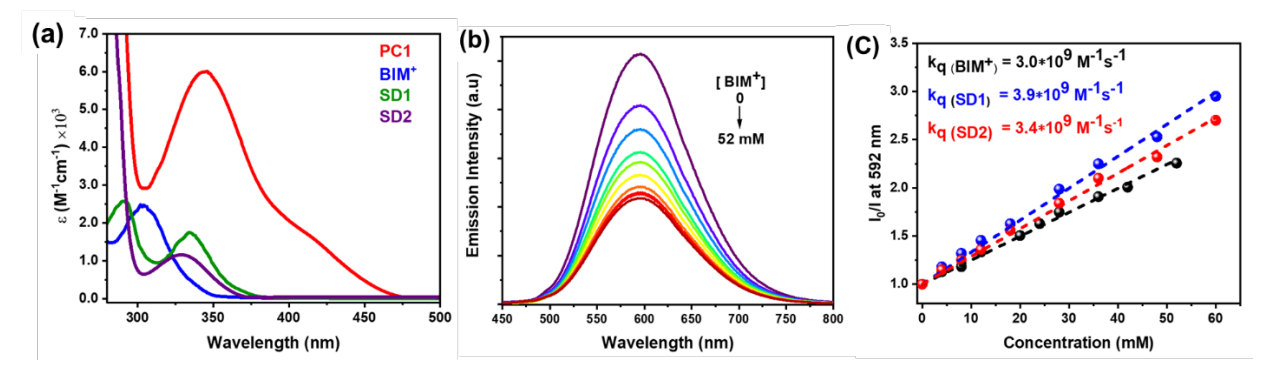


**Figure 1.** (a) UV-visible absorption spectra of PC1 (red), BIM<sup>+</sup> (blue), SD1 (green) and SD2 (violet) in benzene/DMF (1:1) solvent mixture. (b) Steady-state emission spectra of 0.5 mM PC1 containing 0-52 mM (violet-maroon) BIM<sup>+</sup> in benzene/DMF (1:1) solvent mixture. (c) Stern-Volmer plots for PC1 quenching by BIM<sup>+</sup> (black), SD1 (blue) and SD2 (red).

Electrochemical regeneration of BIMH. In a previous study, we showed that the proton-coupled mechanism can be used to achieve the quantitative regeneration of benzimidazole-based hydride donors via an electron-proton-electron transfer mechanism.<sup>8</sup> To evaluate whether the analogous proton-coupled mechanism can be applied to regenerate BIMH from BIM<sup>+</sup>, we investigated the electrochemical reduction of BIM<sup>+</sup> in the presence of a proton source. The choice of the proton source was dictated by the pKa of BIMH<sup>+</sup>, which was calculated to be 16.3 in DMSO.<sup>8</sup> Thus, phenol (pKa = 16.47 in DMSO<sup>40</sup>) was chosen as the optimal proton source for the protonation of one-electron reduced BIM<sup>+</sup>. Figure S5 shows the cyclic voltammograms (CV) of BIM<sup>+</sup> obtained in the presence and absence of phenol. In the absence of phenol, the first reduction of BIM<sup>+</sup> occurs as a chemically reversible peak at -2.1 V vs NHE. The current density approximately doubled in the presence of phenol, indicating that BIMH<sup>+</sup> was protonated and further reduced.<sup>22</sup> Moreover, the formation of BIMH was further confirmed by the appearance of its oxidation peak at 0 V vs NHE in the presence of phenol.

To further confirm the electrochemical regeneration of BIMH from BIM<sup>+</sup>, we performed the controlled-potential electrolysis experiments in DMSO-d<sub>6</sub> at an applied potential of –2.2 V vs NHE (Figure S7). The progress of electrolysis was monitored using <sup>1</sup>H-NMR spectroscopy in the presence of 1,3,5-trimethoxy benzene as an internal standard. The peaks associated with BIM<sup>+</sup> (6.9 and 7.3 ppm) were found to decrease in intensity, while the increase in the peaks (5.4 – 5.7 ppm) corresponding to BIMH occurred over the course of reaction. The conversion occurred with 99 % yield, indicating that the efficient regeneration of BIMH takes place via the proton-coupled mechanism.

Photochemical regeneration of BIMH. The experimental conditions for the photo-regeneration of BIMH were screened to maximize the BIMH yield (see details in methods section). The concentration of PC1 (1.0 mM) was chosen to ensure strong light absorption at 460 nm, where the selective excitation of the photosensitizer can be achieved. The BIMH formation was monitored using <sup>1</sup>H NMR spectroscopy under different reaction conditions, as exemplified in Figure 2. At t=0 days, the NMR spectrum in the 5-7 ppm region consists of signals associated with BIM<sup>+</sup> (6.42 ppm), phenol (6.67 and 6.88 ppm) and PC1 (6.20 ppm). As the photochemical transformation proceeds, the BIM<sup>+</sup> peaks were found to decrease in intensity and a concomitant increase in the intensity of BIMH peaks at 6.12, 6.21. 6.27 and 6.51 ppm were observed. The BIMH peaks in the reaction mixture are slightly shifted relative to those of the reference spectrum, likely due to different polarity of the reaction mixture (containing excess sacrificial donor and phenol) relative to the solvent mixture without additives. In addition, two new peaks appear near the phenol peaks at 6.70 and 6.85 ppm, and those are most likely associated with the phenoxide formed after the proton transfer to BIM radical. To further confirm that the peaks at 6.12, 6.21, 6.27 and 6.51 ppm correspond to BIMH, the final reaction mixture was exposed to air. As expected, the peaks at 6.12, 6.21. 6.27 and 6.51 ppm disappeared because BIMH is unstable in air and oxidizes to BIM<sup>+</sup>. The peaks at 6.70 and 6.85 ppm, assigned here to phenoxide ion, decreased, which is consistent with the protonation of phenoxide ion by moisture from air. The percent conversion of BIM<sup>+</sup> to BIMH was quantified using the DMF peak at 7.20 ppm as an internal standard.

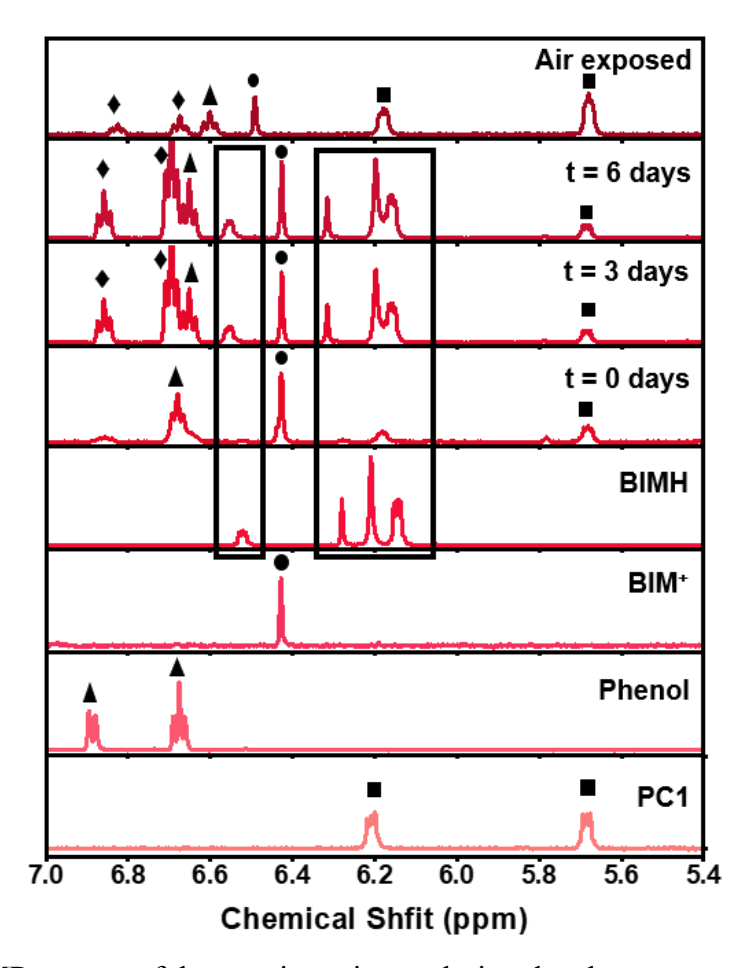


**Figure 2.** <sup>1</sup>H-NMR spectra of the reaction mixture during the photo-regeneration experiment. The reaction mixture contained 1.0 mM PC1, 30.0 mM BIM<sup>+</sup>, 0.3 M SD1, and 0.1 M phenol in DMF-d<sub>7</sub>/benzene-d<sub>6</sub> (1:1 ratio). Sample was irradiated at 460 nm. Peaks inside the boxes indicate the formation of BIMH. Triangle symbols indicate phenol peaks, square symboles indicate PC1 peaks, circle symboles indicate BIM<sup>+</sup> peaks, and diamond symbols indicate unkown peaks (possibly phenoxide ion). The spectra were collected at three time intervals (t = 0, 3 and 6 days). The reference spectra of BIMH, BIM<sup>+</sup>, phenol, and PC1 in benzene-d<sub>6</sub>/DMF-d<sub>7</sub> (1:1) solvent mixture are shown for comparison. The NMR spectrum of the reaction mixture after 6 days, followed by air exposure for 30 hours is shown to confirm the assignment (BIMH is air-sensitive, so it converts back to BIM<sup>+</sup>).

Both SD1 and SD2 yielded the hydride formation (Figure 3a). However, the hydride yields were better for SD1, most likely due to its higher reducing power (Scheme 2). In general, the hydride yield increased as the BIM<sup>+</sup> or SD1/SD2 concentration was increased. For example, the increase in the concentration of BIM<sup>+</sup> from 0.01 M to 0.03 M increased the BIMH yield from 12% to 47% in the presence of 0.2 M SD1. However, further concentration increase was limited by the low solubility of these ions in the solvent mixture. To improve the solubility of sacrificial donors, the counterions for SD1 and SD2 were exchanged from sodium to tetraalkyl ammonium ions. This

approach resulted in an increased solubility of SD1 from 0.06 M to 0.3 M, which improved the hydride yield from 28% to 50% (Figure 3a). The pKa of the proton source had a large effect on the hydride yields (Figure 3b). The best yields were obtained for the proton source with pKa=15.40, while the use of either stronger or weaker acids gave poorer yields. Weaker proton sources are likely not a sufficiently strong acid to protonate the BIM radical. We hypothesize that the stronger acids lead to the protonation of the sacrificial electron donor, lowering its reducing power.

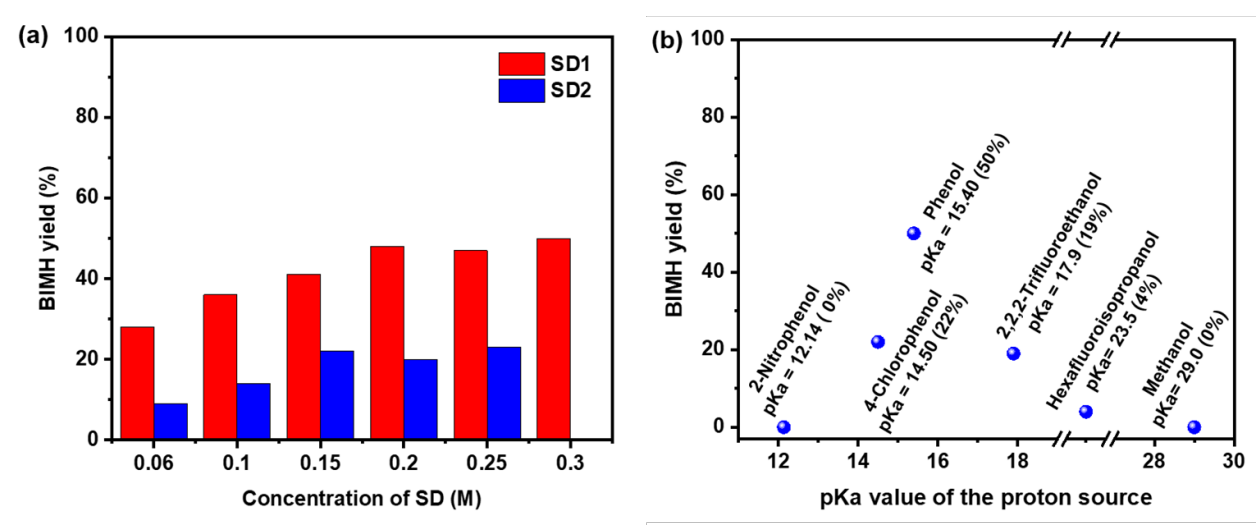


**Figure 3.** BIMH yields after photoregeneration under varying experimental conditions: (a) Different sacrificial donors at varying concentrations were used [SD1] = 0.06 M - 0.3 M (red bars) and [SD2] = 0.06 M - 0.25 M (blue bars). Reaction conditions: [PC1] = 0.001 M, [BIM<sup>+</sup>] = 0.03 M, and [Phenol]= 0.1 M in benzene-d<sub>6</sub>:DMF-d<sub>7</sub> (1:1) solvent mixture. Samples were irradiated at 460 nm for 6 days. (b) Different proton sources were used: pKa values range from 12 to 29 (in DMSO).

The highest yield of BIMH (50%) was achieved in the presence of 0.3 M of SD1, 0.1 M of phenol, and 0.03 M of BIM<sup>+</sup> after 6 days. We were unable to improve the hydride yield beyond this point, most likely due to the formation of the colored by-product during the decomposition of the sacrificial electron donor that acts as a filter and prevents excitation of photocatalysts (PC1) (Figures S9 and S10). The colored product disappears when the reaction mixture is exposed to air and is probably due to S-based radicals formed upon oxidation of thiolates that have not yet dimerized into disulfide products. We anticipate that BIMH yields can be improved in the future by finding a strong reducing sacrificial electron donor that does not form any colored by-product during the reaction.

Time-resolved studies. Femtosecond transient absorption (fsTA) spectroscopy was employed to study the photophysics of PC1 in the absence and presence of BIM<sup>+</sup>, sacrificial electron donor SD1 and/or the proton source phenol (Figure 4, fsTA experiment details can be found in the methods section and S1D). Samples were excited at 430 nm to ensure selective excitation of PC1. The transient signal of PC1 exhibits an excited-state absorption (ESA) feature at 460 nm with additional weaker ESA features below 400 nm and above 600 nm (Figure 4a). The kinetic profiles shown in Figure 4b indicate the presence of a short-lived (few ps) component and another component that lives much longer than the time window of our instrument. Target analysis was applied to experimental data using the sequential A→B model and fits at probe wavelengths 470 and 700 nm are shown in Figure 4b, while the component temporal and spectral profiles are shown in Figure 4c. Assignments of the transient species were made based on photophysical studies of similar phenazine-based photocatalysts reported previously, 41-43 as follows: the initially formed Franck-Condon state (S<sub>FC</sub>) undergoes structural relaxation to the lowest energy singlet state (S<sub>1</sub>) with  $\tau = 2.97$  ps. The S<sub>1</sub> state exhibits charge-transfer character and lives longer than the time window of our instrument. Other photophysical processes (intersystem crossing and triplet relaxation) are observed using nanosecond transient absorption (vide infra). To understand the photophysics involved during catalysis, four samples were prepared for transient absorption measurement: 1) PC1 alone, 2) PC1 in the presence of the electron-acceptor BIM<sup>+</sup>, 3) PC1 in the presence of BIM<sup>+</sup> and the proton source phenol and 4) PC1 in the presence of the sacrificial electron donor SD1. All four samples explored in this study show very similar kinetics in the femtosecond to nanosecond time regime (Figure 4d), indicating that electron and proton transfer events occur on longer timescales. This result is consistent with the relatively low concentration of additives (BIM<sup>+</sup>, phenol and SD1) and with the emission quenching measurements discussed above. At these concentrations, diffusion of the additives to PC1 is not expected to occur on subnanosecond timescales.

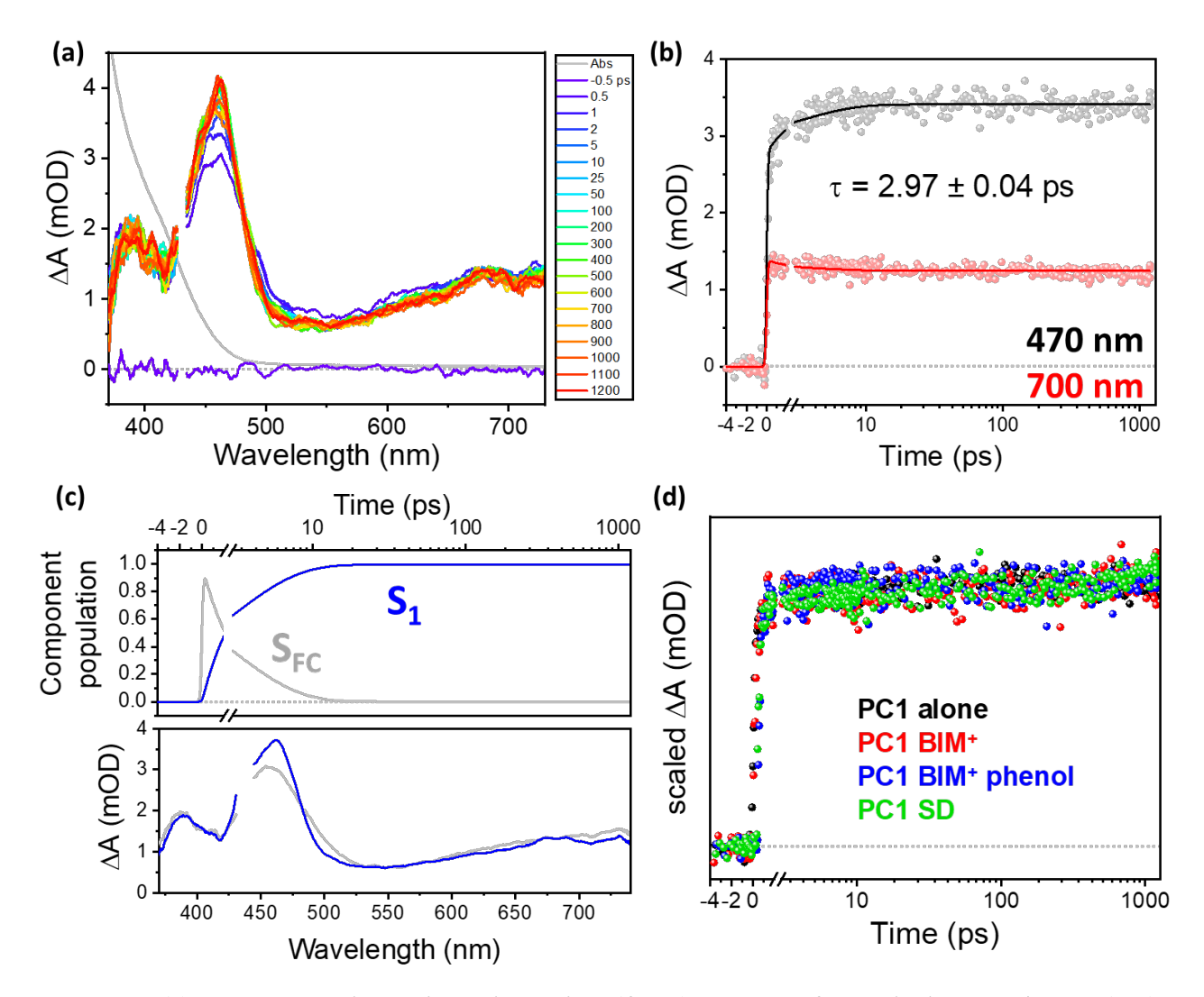


**Figure 4.** (a) Femtosecond transient absorption (fsTA) spectra of PC1 in benzene/DMF (1:1) solvent mixture. The ground-state absorption of the solution is shown in grey for reference. Sample was excited at 430 nm. (b) Kinetic traces at selected wavelengths: 470 nm (black) and 700 nm (red). Dots represent experimental data, while solid lines represent the fit using the sequential A→B model. (c) Component spectra (top) and time-dependent evolution of component population (bottom) obtained from target analysis. (d) Comparison of kinetics at 450 nm for PC1 alone (black), PC1 in the presence of 25 mM BIM<sup>+</sup> (red), PC1 in the presence of 25 mM BIM<sup>+</sup> and 30 mM phenol (blue), and PC1 in the presence of 60 mM SD1. The concentration of PC1 in all samples was 2.5 mM.

The photochemical events were further studied at longer timescales using ns transient absorption spectroscopy (nsTA, Figures 5 and S12). Figure 5 shows the nsTA spectra of PC1 collected in the absence and the presence of BIM<sup>+</sup>. The spectra collected for PC1 alone near time zero (instrument response function is ~1 ns) consist of two positive features with maxima at 460 and 750 nm. These transient features match the spectrum obtained at the end of the fsTA experiment (Figure 4) and

are assigned to the  $S_1$  state of PC1. The  $S_1$  state decays with the lifetime of  $\tau_1$  = 17.1 ns to generate the new transient feature with absorption at 450 nm (Figure 5c). This transient is long-lived ( $\tau_2$  = 4.13 µs) and readily quenched by molecular oxygen, suggesting that it is associated with the triplet excited state  $T_1$  of PC1. Our assignment is consistent with the previous nanosecond TA involving similar derivatives.<sup>27,29</sup>

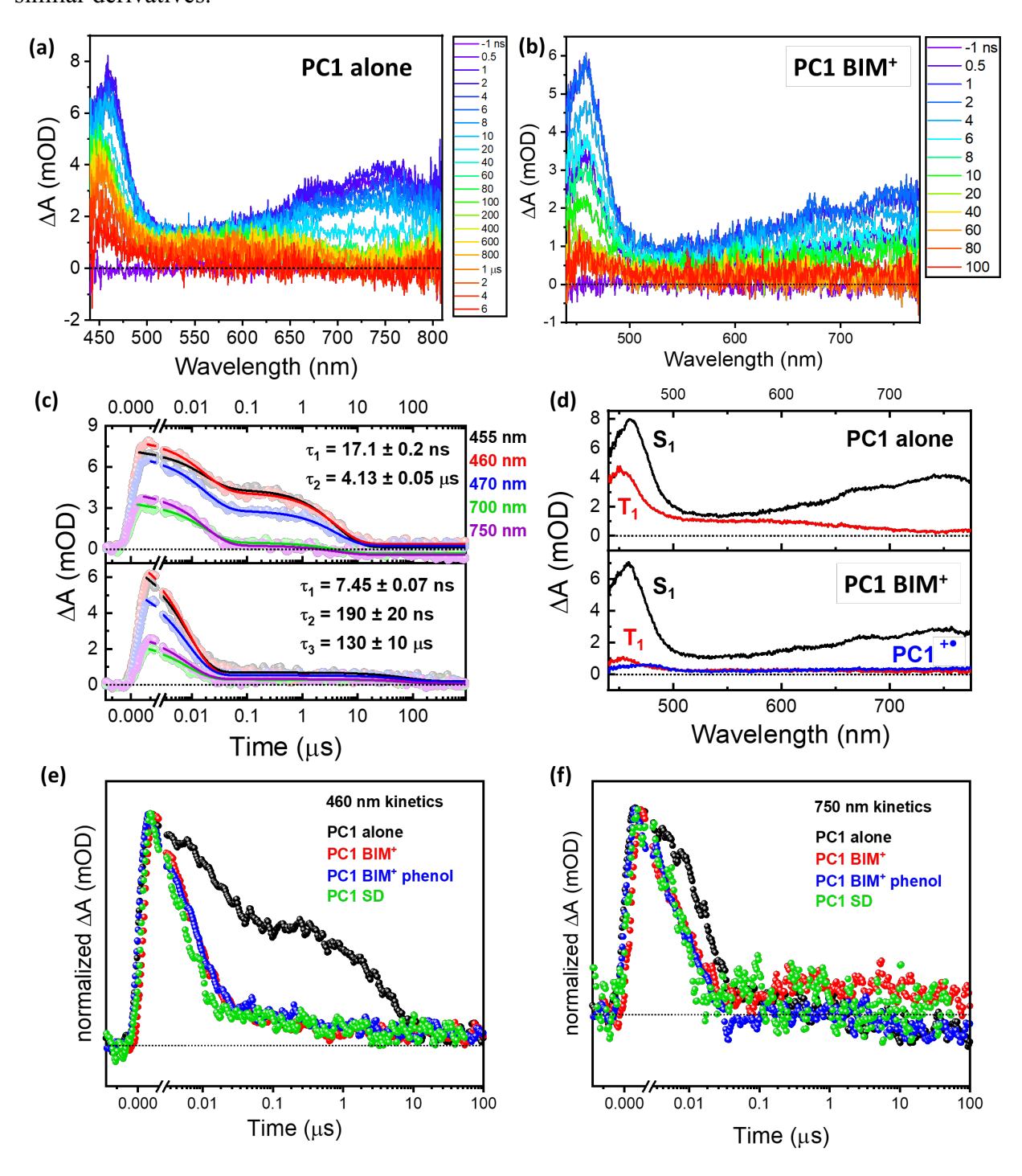


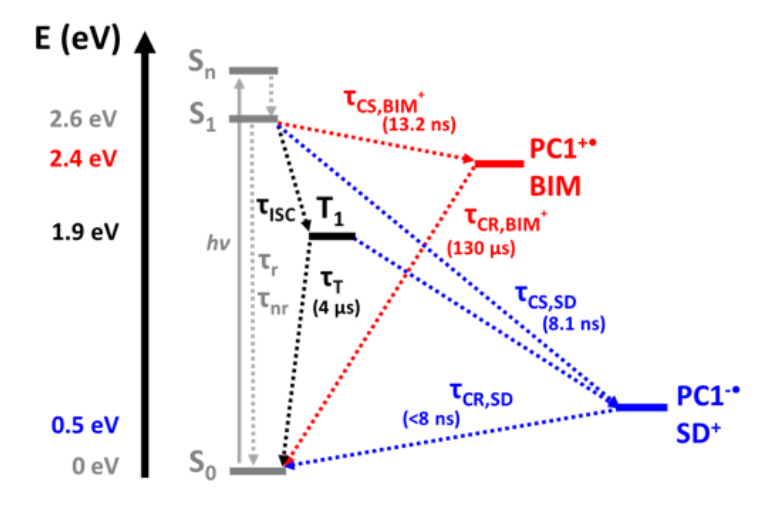
**Figure 5.** Nanosecond transient absorption spectra of (a) PC1 alone and (b) PC1 BIM<sup>+</sup> after 430 nm excitation. (c) Kinetic traces at selected wavelengths of PC1 alone (top) and PC1 BIM<sup>+</sup> (bottom). (d) Spectral profiles of S<sub>1</sub> and T<sub>1</sub> states of PC1 alone (top) and S<sub>1</sub>, T<sub>1</sub>, and PC1<sup>+</sup> states of PC1 BIM<sup>+</sup> (bottom) calculated from principal component analysis. e) Normalized nsTA kinetics at 460 nm of all four samples explored in this study. f) Normalized nsTA kinetics at 750 nm.

In the presence of BIM<sup>+</sup> (Figure 5b) the singlet excited-state lifetime was found to shorten to 7.5 ns, which is consistent with the fluorescence quenching observed for PC1 in the presence of BIM<sup>+</sup> (Figure 1). This excited-sate lifetime shortening is assigned to the photoinduced electron transfer from S<sub>1</sub> state of PC1 to BIM<sup>+</sup>, based on the thermodynamic arguments illustrated in Scheme 2. Target analysis of the nsTA spectra using a  $0 \rightarrow 1 \rightarrow 2 \rightarrow 0$ ,  $1 \rightarrow 3 \rightarrow 0$  sequential/parallel hybrid model reveal two additional spectral features with lifetimes of  $\tau_2 = 190$  ns and  $\tau_3 = 130$  µs. We assign these species to the  $T_1$  excited state of PC1 ( $\tau_2$ ) and the PC1<sup>+</sup>• radical cation ( $\tau_3$ ). The  $\tau_2$ component resembles spectrally the T<sub>1</sub> state of PC1, but with a shorter lifetime (Figure 5d). The long-lived τ<sub>3</sub> component resembles PC1<sup>•+</sup> measured using UV/Vis spectroelectrochemistry (Figures S11 and S14). Other transients that are formed during the photoinduced electron transfer do not absorb in the spectral range of our probe pulse (spectroelectrochemical data of BIM+/BIM. Conversion are shown in Figure S13). This final component decays with  $\tau_3 = 130 \,\mu s$ , which we assign as charge recombination with BIM radical to recover the starting materials (see Scheme 3). Such a long-lived charge-separated state is ideal for photocatalysis. Based on our spectroscopic findings, we propose the kinetic model as described in Scheme 3. In the absence of BIM<sup>+</sup>, the relaxation of the initially generated PC1 excited state involves the formation of a charge-transfer  $S_1$  state that undergoes radiative decay and intersystem crossing with a 17 ns lifetime. The  $T_1$  state is formed, which then decays to the ground state with a 4 µs lifetime. In the presence of BIM<sup>+</sup>, the deactivation of S<sub>1</sub> state involves a competition between radiative decay plus intersystem crossing (17 ns lifetime) and electron transfer to BIM<sup>+</sup> (13 ns) lifetime, resulting in an overall 56% conversion of photoexcited PC1 to PC1. The shortening of the T<sub>1</sub> state of PC1 in the presence of BIM<sup>+</sup> is not well understood at this point, since the T<sub>1</sub> state of PC1 is not predicted to be sufficiently reducing to enable photoinduced electron transfer to BIM<sup>+</sup> (Scheme 2). However, the 700 and 750 nm kinetic traces for PC1 with BIM<sup>+</sup> clearly show a concomitant rise with 190 ns, suggesting that the T<sub>1</sub> state of PC1 may actually be capable of reducing BIM<sup>+</sup> to BIM<sup>•</sup>. The photogenerated radicals PC1<sup>•+</sup> and BIM<sup>•</sup> undergo charge recombination with the lifetime of 130 μs.

The nsTA spectra of PC1 in the presence of BIM<sup>+</sup> and phenol are shown in Figures S15 and S16. The target analysis reveals the presence of the same intermediates  $(S_1/T_1 \text{ states of PC1} \text{ and the ground doublet state of PC1}^{\bullet+})$ , indicating that the same photoinduced electron transfer from the  $S_1$  state of PC1 takes place in the presence of phenol. Furthermore, the observed time constants are unaffected by phenol, given the low signals of the  $T_1$  and PC1 $^{\bullet+}$  components in the PC1 with BIM<sup>+</sup> and PC1 with BIM<sup>+</sup> and phenol nsTA datasets. While thermodynamic arguments (Scheme 2) suggest the proton-coupled electron transfer PC1 $(S_1)$  + BIM<sup>+</sup> + PhOH  $\Rightarrow$  PC1 $^{\bullet+}$  + BIMH $^{\bullet+}$  + PhO $^-$  is expected to be a spontaneous process, the likely diffusion-limited charge separation and recombination dynamics obscure the role of PCET in this system.

The nsTA kinetics of PC1 in the presence of SD1 are shown in Figures S15 and S16. The global analysis of the data indicates that only S<sub>1</sub> and T<sub>1</sub> states are detected as transients. Surprisingly, no accumulation of the charge-separated species was observed, indicating that either PC1 •- is not observed in our probe region or the charge recombination between PC<sup>•-</sup> and SD<sup>•</sup> is faster than the rate of charge separation. We conclude, however, that rapid charge recombination is more likely since PC<sup>•-</sup> is expected to absorb near 550 nm. <sup>48</sup> Since the presence of SD1 shortens the S<sub>1</sub> lifetimes and since no radical ion intermediates are detected, we postulate that the photoinduced electron transfer from SD1 to the S<sub>1</sub> state of PC1 takes place with the lifetime of 8 ns, and that it is followed by a rapid charge recombination, preventing the detectable accumulation of radicals. Such fast recombination appears to outcompete the subsequent degradation of the oxidized sacrificial donor. After PET, the oxidation of SD<sup>-</sup> is expected to form neutral SD<sup>•</sup> radical, which dimerizes to form D1S-SD1 (SD1 dimer).<sup>49</sup> Given that the charge recombination is very fast, we conclude that the reaction between photoexcited PC1 and the sacrificial donor does not lead to productive photochemistry. Instead, we propose that the productive photochemistry involves the photoinduced electron transfer from PC1 to BIM<sup>+</sup> (Scheme 2). The sacrificial donor is likely to act as a productive sacrificial donor in the dark reaction:  $PC1^{\bullet+} + SD1^{-} \rightarrow PC1 + SD1^{\bullet}$ . Additionally, the T<sub>1</sub> state of PC1 is observed in the PC1 with SD1 nsTA measurement (Figures S15 and S16). Similar to the observed T<sub>1</sub> states in the PC1 with BIM<sup>+</sup> and PC1 with BIM<sup>+</sup> and phenol samples, the T<sub>1</sub> state of PC1 decays more rapidly than in PC1 only, 0.8 μs vs 4 μs, respectively (Scheme 4). The accelerated decay of the T<sub>1</sub> state of PC1 indicates that the T<sub>1</sub> state is quenched by electron transfer from SD1, similar to the S<sub>1</sub> state of PC1. Participation of the T<sub>1</sub> state of PC1 in the photoinduced electron transfer reactions with BIM+ and SD1, as the nsTA data suggests, would further increase the hydride regeneration yield and offset some of the losses associated with the slower diffusion-limited processes.

**Scheme 4.** Energy diagram describing the nanosecond kinetics of PC1 in the presence of 25 mM BIM<sup>+</sup> and 60 mM SD1.



#### **Conclusion**

In summary, we report a study of the metal-free system for photochemical hydride transfer reactions. The photocatalyst consists of an organic phenazine-based chromophore and an organic hydride donor composed of the bioinspired benzoimidazole motif. The photo-regeneration of the hydride was achieved with a decent yield (50%) and further improvements are anticipated with improved selection of sacrificial electron donors. Our time-resolved measurements indicate that the photoinduced electron transfer from the sacrificial electron donor does not generate long-lived radical intermediates and that the observed photochemistry is instead initiated by the photoinduced electron transfer from excited PC1 to BIM<sup>+</sup>. The unproductive quenching by the sacrificial electron donors may also be improved by changing the sacrificial electron donor used. Finding a sacrificial electron donor that does not form a colored product upon electron transfer to PC1 is vital to prevent masking the excitation of PC1 to regenerate the BIMH. We anticipate that these earth-abundant chromophores and catalysts will be important molecular building blocks for photosynthesis applications, such as the reduction of carbon dioxide and other compounds.

# **Supporting Information**

Details on steady-state spectroscopy, electrochemistry, photochemical regeneration of BIMH and transient absorption spectroscopy. This material is available free of charge via the Internet at <a href="https://pubs.acs.org">https://pubs.acs.org</a>.

## Acknowledgements

This work was supported by the National Science Foundation (NSF 1954298) This work is partly supported by the U.S. Department of Energy (DOE), Office of Science, Office of Basic Energy Science, Division of Chemical Sciences, Geosciences and Biosciences, through Argonne National Laboratory under Contract No. DE-AC02-06CH11357.

#### References

- (1) Blankenship, R. E. *Molecular Mechanisms of Photosynthesis*; John Wiley & Sons, 2014.
- (2) Hou, H. J. M.; Najafpour, M. M.; Moore, G. F.; Allakhverdiev, S. I. *Photosynthesis: Structures, Mechanisms, and Applications*; Springer, 2017; Vol. 417.
- (3) Mayr, P.; Nidetzky, B. Catalytic Reaction Profile for NADH-Dependent Reduction of Aromatic Aldehydes by Xylose Reductase from Candida Tenuis. *Biochem. J.* 2002, 366 (3), 889–899.
- (4) Bornscheuer, U. T.; Huisman, G. W.; Kazlauskas, R. J.; Lutz, S.; Moore, J. C.; Robins, K. Engineering the Third Wave of Biocatalysis. *Nature* **2012**, *485* (7397), 185–194.
- Ouellet, S. G.; Walji, A. M.; Macmillan, D. W. C. Enantioselective Organocatalytic Transfer Hydrogenation Reactions Using Hantzsch Esters. *Acc. Chem. Res.* **2007**, *40* (12), 1327–1339.
- (6) Zheng, C.; You, S. L. Transfer Hydrogenation with Hantzsch Esters and Related Organic Hydride Donors. *Chemical Society Reviews*. 2012, pp 2498–2518. https://doi.org/10.1039/c1cs15268h.
- (7) Stephan, D. W.; Erker, G. Frustrated Lewis Pairs: Metal-free Hydrogen Activation and More. *Angew. Chemie Int. Ed.* **2010**, *49* (1), 46–76.
- (8) Ilic, S.; Alherz, A.; Musgrave, C. B.; Glusac, K. D. Importance of Proton-Coupled Electron Transfer in Cathodic Regeneration of Organic Hydrides. *Chem. Commun.* **2019**, *55* (39), 5583–5586.
- (9) Kim, J.; Lee, S. H.; Tieves, F.; Choi, D. S.; Hollmann, F.; Paul, C. E.; Park, C. B. Biocatalytic C= C Bond Reduction through Carbon Nanodot-Sensitized Regeneration of NADH Analogues. *Angew. Chemie Int. Ed.* 2018, 57 (42), 13825–13828.
- (10) Wei, J.; Zhao, L.; He, C.; Zheng, S.; Reek, J. N. H.; Duan, C. Metal–Organic Capsules with NADH Mimics as Switchable Selectivity Regulators for Photocatalytic Transfer Hydrogenation. *J. Am. Chem. Soc.* **2019**, *141* (32), 12707–12716.

- (11) Tensi, L.; Macchioni, A. Extremely Fast NADH-Regeneration Using Phosphonic Acid as Hydride Source and Iridium-Pyridine-2-Sulfonamidate Catalysts. ACS Catal. 2020, 10 (14), 7945–7949.
- (12) Wu, Y.; Shi, J.; Li, D.; Zhang, S.; Gu, B.; Qiu, Q.; Sun, Y.; Zhang, Y.; Cai, Z.; Jiang, Z. Synergy of Electron Transfer and Electron Utilization via Metal–Organic Frameworks as an Electron Buffer Tank for Nicotinamide Regeneration. ACS Catal. 2020, 10 (5), 2894–2905.
- (13) Brown, K. A.; Wilker, M. B.; Boehm, M.; Hamby, H.; Dukovic, G.; King, P. W. Photocatalytic Regeneration of Nicotinamide Cofactors by Quantum Dot–Enzyme Biohybrid Complexes. *ACS Catal.* **2016**, *6* (4), 2201–2204.
- (14) Song, H.; Lee, S. H.; Won, K.; Park, J. H.; Kim, J. K.; Lee, H.; Moon, S.; Kim, D. K.; Park, C. B. Electrochemical Regeneration of NADH Enhanced by Platinum Nanoparticles. *Angew. Chemie Int. Ed.* **2008**, *47* (9), 1749–1752.
- (15) Okamoto, Y.; Köhler, V.; Paul, C. E.; Hollmann, F.; Ward, T. R. Efficient in Situ Regeneration of NADH Mimics by an Artificial Metalloenzyme. *ACS Catal.* **2016**, *6* (6), 3553–3557.
- (16) Ilic, S.; Alherz, A.; Musgrave, C. B.; Glusac, K. D. Thermodynamic and Kinetic Hydricities of Metal-Free Hydrides. *Chem. Soc. Rev.* **2018**, *47* (8), 2809–2836.
- (17) Cukier, R. I.; Nocera, D. G. Proton-Coupled Electron Transfer. *Annu. Rev. Phys. Chem.*1998, 49 (1), 337–369.
- (18) Weinberg, D. R.; Gagliardi, C. J.; Hull, J. F.; Murphy, C. F.; Kent, C. A.; Westlake, B. C.; Paul, A.; Ess, D. H.; McCafferty, D. G.; Meyer, T. J. Proton-Coupled Electron Transfer. *Chem. Rev.* **2012**, *112* (7), 4016–4093.
- (19) Hollmann, F.; Witholt, B.; Schmid, A. [Cp\* Rh (Bpy)(H2O)] 2+: A Versatile Tool for Efficient and Non-Enzymatic Regeneration of Nicotinamide and Flavin Coenzymes. *J. Mol. Catal. B Enzym.* **2002**, *19*, 167–176.
- (20) Tsay, C.; Livesay, B. N.; Ruelas, S.; Yang, J. Y. Solvation Effects on Transition Metal Hydricity. *J. Am. Chem. Soc.* **2015**, *137* (44), 14114–14121.
- (21) Ilic, S.; Pandey Kadel, U.; Basdogan, Y.; Keith, J. A.; Glusac, K. D. Thermodynamic Hydricities of Biomimetic Organic Hydride Donors. *J. Am. Chem. Soc.* **2018**, *140* (13), 4569–4579.

- (22) Lim, C.-H.; Ilic, S.; Alherz, A.; Worrell, B. T.; Bacon, S. S.; Hynes, J. T.; Glusac, K. D.; Musgrave, C. B. Benzimidazoles as Metal-Free and Recyclable Hydrides for CO2 Reduction to Formate. *J. Am. Chem. Soc.* **2018**, *141* (1), 272–280.
- (23) Weerasooriya, R. B.; Gesiorski, J. L.; Alherz, A.; Ilic, S.; Hargenrader, G. N.; Musgrave,
  C. B.; Glusac, K. D. Kinetics of Hydride Transfer from Catalytic Metal-Free Hydride
  Donors to CO2. *J. Phys. Chem. Lett.* 2021, *12*, 2306–2311.
- Hargenrader, G. N.; Weerasooriya, R. B.; Ilic, S.; Niklas, J.; Poluektov, O. G.; Glusac, K.
   D. Photoregeneration of Biomimetic Nicotinamide Adenine Dinucleotide Analogues via a
   Dye-Sensitized Approach. ACS Appl. Energy Mater. 2018, 2 (1), 80–91.
- (25) Ilic, S.; Brown, E. S.; Xie, Y.; Maldonado, S.; Glusac, K. D. Sensitization of P-Gap with Monocationic Dyes: The Effect of Dye Excited-State Lifetime on Hole Injection Efficiencies. *J. Phys. Chem. C* **2016**, *120* (6), 3145–3155.
- (26) Theriot, J. C.; Lim, C.-H.; Yang, H.; Ryan, M. D.; Musgrave, C. B.; Miyake, G. M. Organocatalyzed Atom Transfer Radical Polymerization Driven by Visible Light. *Science* (80-.). **2016**, 352 (6289), 1082–1086.
- (27) Du, Y.; Pearson, R. M.; Lim, C.-H.; Sartor, S. M.; Ryan, M. D. M. D.; Yang, H.; Damrauer, N. H.; Miyake, G. M. Strongly Reducing Visible Light Organic Photoredox Catalysts as Sustainable Alternatives to Precious Metals. *Chemistry* 2017, 23 (46), 10962.
- (28) Ryan, M. D.; Theriot, J. C.; Lim, C.; Yang, H.; G. Lockwood, A.; Garrison, N. G.; Lincoln, S. R.; Musgrave, C. B.; Miyake, G. M. Solvent Effects on the Intramolecular Charge Transfer Character of N, N-diaryl Dihydrophenazine Catalysts for Organocatalyzed Atom Transfer Radical Polymerization. *J. Polym. Sci. Part A Polym. Chem.* **2017**, *55* (18), 3017–3027.
- (29) Lee, J.; Shizu, K.; Tanaka, H.; Nakanotani, H.; Yasuda, T.; Kaji, H.; Adachi, C. Controlled Emission Colors and Singlet–Triplet Energy Gaps of Dihydrophenazine-Based Thermally Activated Delayed Fluorescence Emitters. *J. Mater. Chem. C* **2015**, *3* (10), 2175–2181.
- (30) Lim, C.-H.; Ryan, M. D.; McCarthy, B. G.; Theriot, J. C.; Sartor, S. M.; Damrauer, N. H.; Musgrave, C. B.; Miyake, G. M. Intramolecular Charge Transfer and Ion Pairing in N, N-Diaryl Dihydrophenazine Photoredox Catalysts for Efficient Organocatalyzed Atom Transfer Radical Polymerization. *J. Am. Chem. Soc.* 2017, 139 (1), 348–355.

- (31) Lewis, S. E.; Wilhelmy, B. E.; Leibfarth, F. A. Organocatalytic C–H Fluoroalkylation of Commodity Polymers. *Polym. Chem.* **2020**, *11* (30), 4914–4919.
- (32) Rao, H.; Lim, C.-H.; Bonin, J.; Miyake, G. M.; Robert, M. Visible-Light-Driven Conversion of CO2 to CH4 with an Organic Sensitizer and an Iron Porphyrin Catalyst. *J. Am. Chem. Soc.* **2018**, *140* (51), 17830–17834.
- (33) Pavlishchuk, V. V; Addison, A. W. Conversion Constants for Redox Potentials Measured versus Different Reference Electrodes in Acetonitrile Solutions at 25 C. *Inorganica Chim. Acta* **2000**, *298* (1), 97–102.
- (34) Hayes, D.; Kohler, L.; Hadt, R. G.; Zhang, X.; Liu, C.; Mulfort, K. L.; Chen, L. X. Excited State Electron and Energy Relays in Supramolecular Dinuclear Complexes Revealed by Ultrafast Optical and X-Ray Transient Absorption Spectroscopy. *Chem. Sci.* **2018**, *9* (4), 860–875.
- (35) McCarthy, B.; Sartor, S.; Cole, J.; Damrauer, N.; Miyake, G. M. Solvent Effects and Side Reactions in Organocatalyzed Atom Transfer Radical Polymerization for Enabling the Controlled Polymerization of Acrylates Catalyzed by Diaryl Dihydrophenazines. *Macromolecules* **2020**, *53* (21), 9208–9219.
- (36) Brevet, D.; Mugnier, Y.; Samreth, S. Réactivité Du Bromure de 5-Thioxylopyranosyle et Du 1, 5-Dithioxylopyranoside Vis-à-Vis d'anions Thiolate. *Comptes Rendus Chim.* **2003**, *6* (4), 485–491.
- (37) Pellegrin, Y.; Odobel, F. Sacrificial Electron Donor Reagents for Solar Fuel Production. *Comptes Rendus Chim.* **2017**, *20* (3), 283–295.
- (38) Presti, D.; Truhlar, D. G.; Gagliardi, L. Intramolecular Charge Transfer and Local Excitation in Organic Fluorescent Photoredox Catalysts Explained by RASCI-PDFT. *J. Phys. Chem. C* **2018**, *122* (22), 12061–12070.
- (39) Lim, C. H.; Ryan, M. D.; McCarthy, B. G.; Theriot, J. C.; Sartor, S. M.; Damrauer, N. H.; Musgrave, C. B.; Miyake, G. M. Intramolecular Charge Transfer and Ion Pairing in N, N-Diaryl Dihydrophenazine Photoredox Catalysts for Efficient Organocatalyzed Atom Transfer Radical Polymerization. *J. Am. Chem. Soc.* 2017, 139 (1), 348–355. https://doi.org/10.1021/jacs.6b11022.
- (40) Roy, K.; Popelier, P. L. A. Predictive QSPR Modeling of the Acidic Dissociation Constant (PKa) of Phenols in Different Solvents. *J. Phys. Org. Chem.* **2009**, *22* (3), 186–

196.

- (41) Sartor, S. M.; Lattke, Y. M.; McCarthy, B. G.; Miyake, G. M.; Damrauer, N. H. Effects of Naphthyl Connectivity on the Photophysics of Compact Organic Charge-Transfer Photoredox Catalysts. *J. Phys. Chem. A* 2019, *123* (22), 4727–4736.
- (42) Sartor, S. M.; Chrisman, C. H.; Pearson, R. M.; Miyake, G. M.; Damrauer, N. H. Designing High-Triplet-Yield Phenothiazine Donor–Acceptor Complexes for Photoredox Catalysis. *J. Phys. Chem. A* **2020**, *124* (5), 817–823.
- (43) Sartor, S. M.; McCarthy, B. G.; Pearson, R. M.; Miyake, G. M.; Damrauer, N. H. Exploiting Charge-Transfer States for Maximizing Intersystem Crossing Yields in Organic Photoredox Catalysts. *J. Am. Chem. Soc.* **2018**, *140* (14), 4778–4781.
- (44) Rabe, E. J.; Corp, K. L.; Sobolewski, A. L.; Domcke, W.; Schlenker, C. W. Proton-Coupled Electron Transfer from Water to a Model Heptazine-Based Molecular Photocatalyst. *J. Phys. Chem. Lett.* **2018**, *9* (21), 6257–6261.
- (45) Rabe, E. J.; Corp, K. L.; Huang, X.; Ehrmaier, J.; Flores, R. G.; Estes, S. L.; Sobolewski, A. L.; Domcke, W.; Schlenker, C. W. Barrierless Heptazine-Driven Excited State Proton-Coupled Electron Transfer: Implications for Controlling Photochemistry of Carbon Nitrides and Aza-Arenes. *J. Phys. Chem. C* 2019, *123* (49), 29580–29588.
- (46) Reimers, J. R.; Cai, Z.-L. Hydrogen Bonding and Reactivity of Water to Azines in Their S 1 (n, Π\*) Electronic Excited States in the Gas Phase and in Solution. *Phys. Chem. Chem. Phys.* **2012**, *14* (25), 8791–8802.
- (47) Eisenhart, T. T.; Dempsey, J. L. Photo-Induced Proton-Coupled Electron Transfer Reactions of Acridine Orange: Comprehensive Spectral and Kinetics Analysis. *J. Am. Chem. Soc.* **2014**, *136* (35), 12221–12224.
- (48) Pedersen, S. U.; Christensen, T. B.; Thomasen, T.; Daasbjerg, K. New Methods for the Accurate Determination of Extinction and Diffusion Coefficients of Aromatic and Heteroaromatic Radical Anions in N, N-Dimethylformamide. *J. Electroanal. Chem.* **1998**, 454 (1–2), 123–143.
- (49) Witt, D. Recent Developments in Disulfide Bond Formation. *Synthesis (Stuttg).* **2008**, 2008 (16), 2491–2509.

# **TOC Graphic**

